Materials Research. 2026; 29: e20250639
DOI: https://doi.org/10.1590/1980-5373-MR-2025-0639

Influence of the Phase Morphologies on Pitting Resistance in Different Regions of the Heat-Affected Zone in GMAW Welds of Duplex Stainless Steel UNS S31803(2205)

A. Cruz-Crespo[a], E.V. Morales[b,c,], J.V.M. Oria[a], J.A. Pozo Morejón[a], I. S. Bott[d], L.S. Araujo[b]*

[a]*Universidad Central "Marta Abreu" de Las Villas, Centro de Investigaciones de Soldadura, Santa Clara, Villa Clara, Cuba.*
[b]*Universidade Federal do Rio de Janeiro, Escola Politécnica, Programa de Engenharia Metalúrgica e de Materiais, Rio de Janeiro, RJ, Brasil.*
[c]*Universidad Central "Marta Abreu" de Las Villas, Departamento de Física, Santa Clara, Villa Clara, Cuba.*
[d]*Pontifícia Universidade Católica do Rio de Janeiro, Departamento de Engenharia Química e de Materiais, Rio de Janeiro, RJ, Brasil.*

Received: August 15, 2025; Revised: March 06, 2026; Accepted: April 08, 2026

Three different regions in the heat-affected zone are formed when the shielding gas mixture during the GMAW procedure is argon-rich. The microstructural characterization and corrosion susceptibility of different heat-affected zone (HAZ) regions in welds of UNS S31803(2205) duplex stainless steel (DSS), were evaluated by optical images, scanning electron microscopy and transmission electron microscopy. The pitting susceptibility of the different regions in the HAZ was evaluated by pitting corrosion tests in an acidified ferric chloride solution. The analyzed HAZ regions showed different HAZ dimensions and microstructural aspects as grain size, phase fractions, morphologies and compositions that influenced the pitting resistance. The HAZ region induced by the lower cooling rate showed larger ferrite grain size. In this region, the Widmanstätten and intragranular austenite fractions were higher, indicating greater susceptibility to pitting corrosion. The weld with the highest heat input showed the lowest resistance to pitting corrosion.

Keywords: *Duplex stainless-steel, GMAW, Heat-affected zone, Pitting corrosion, Austenite morphologies.*

1. Introduction

Duplex stainless steels show optimized properties for a 50:50 ferrite/austenite ratio[1]. Literature[2-6] has showed the effect of thermal cycles on the HAZ microstructure, describing that an increase in the cooling time favors ferrite grain growth and an increase in austenite content. The effect of the cooling time on the austenite morphologies (grain boundary austenite (GBA), Widmanstätten austenite (WA) and intragranular austenite (IGA)), has also been qualitatively reported[7,8].

The ferrite-austenite transformation causes the partitioning of alloying elements[9]. Therefore, GBA exhibits a more balanced composition than nucleated IGA at lower temperatures after WA formation[1,4-6,10].

As a result of poor partitioning at high cooling rates, ferrite becomes saturated with N while the austenite is enriched in Cr and Mo. The low nitrogen solubility in ferrite favors the chromium nitride (Cr_2N) precipitation[2-4,7,11-13]. At high cooling rates, the CrN may also appear[2,4,12,13]. Many investigations show that nitride precipitation is a common cause for initiating pitting corrosion[3,4,6,7,12]. The cooling rate also influences the formation of the Sigma (σ) phase, affecting corrosion resistance. As σ forms at very slow cooling rates, its presence in welds is unlikely[12,14-16].

To estimate the susceptibility of the HAZ to pitting corrosion, the Pitting Corrosion Resistance Equivalent Number (PREN) can be used. The PREN is based solely on the chemical composition of the phases[4,15,17]. Potentiodynamic tests are then used given the nature of PREN[3,4,6,7,12,15-20]. For welds, literature reports the immersion test in ferric chloride solution[15,16,19,21]. This permits the evaluation of welds for pitting corrosion without the need of specialized equipments[22].

It is often assumed that the heat input during welding fully characterizes all subzones or regions of the heat-affected zone (HAZ) during a welding process. However, this overlooks that certain welding processes can produce subzones with distinct microstructures and properties. In particular, when the shielding gas mixture in gas metal arc welding (GMAW) process is argon-rich, the weld bead cross section exhibits an inflection at the fusion line[20]. This is consequence of different cooling rates in different regions of the HAZ along the fusion line. The morphological changes of austenite within each region of the heat-affected zone (HAZ) that result from different cooling rates during this welding process have not been evaluated in the literature, to the authors' knowledge. Therefore, the present study examines how the local cooling rates influence in the microstructure and pitting corrosion resistance of different HAZ regions in GMAW-welds in the UNS S31803(2205) duplex stainless steel.

*e-mail: evmorales2015@gmail.com
Associate Editor: Hugo Sandim.
Editor-in-Chief: Luiz Antonio Pessan.

2. Materials and Experimental Procedures

Table 1 shows the composition of the base metal and the consumable Sandvik 22.8.3.L wire (AWS ER2209).

Single-pass bead-on-plate GMAW welds were made in sheets (300x150x10 mm) of the UNS S31803(2205) DSS. Single-pass weld was performed to avoid the formation of secondary austenite and unwanted intermetallic phases that can occur in multi-pass welds. The welding process was performed with an electrode of Ø=1.2 mm using direct current with reverse polarity in constant current mode. The shielding gas was 98% Ar + 2% CO_2 at 18 l/min. The nozzle-piece distance was 19 mm. Two heat inputs (1.5 and 2.5 kJ/mm) were used. The arc current and voltage values were 180 A and 24 V. The welding speeds were 2.3 mm/s and 1.38 mm/s for the heat inputs of 1.5 kJ/mm and 2.5 kJ/mm, respectively.

Cross-section samples of the weld were taken for the metallography analysis, with standard preparation and etched with Beraha reagent by ~30 s according to ASTM E3-11[23]. The microstructure was observed by optical microscopy (OM) and scanning electron microscopy (Tescan SEM equipped with a Quantax Microanalysis System using the Spirit Compact Interface). The phase fractions were determined by area percentage using the ImageJ software. EDS/SEM semi quantitative analysis was performed for the composition of each region in the HAZ.

Thin foils for transmission electron microscopy (TEM-JEOL 2010 operated at 200 KV and TEM-STEM Talos F200XG2-Thermo Fisher Scientific) were taken from two HAZ regions of the welded sample with 1.5 kJ/mm and electropolished in a Tenupol-5 (10% perchloric acid/ 90% ethylic alcohol at 0 °C and 20 V).

An acidified chloride solution (6% FeCl3 + 1% HCl), recommended in the ASTM G 48 standard for methods C to F[22], was utilized to produce pits in the heat-affected zone (HAZ) regions during the immersion corrosion tests. Immersion tests were performed at room temperature for 72 h. Three samples were tested for each welding input energy condition. Prior to the immersion corrosion test, the samples were carefully embedded in epoxy resin with 2.9 cm^2 and 3.3 cm^2 of exposed surface areas corresponding to the welded samples with 1.5 kJ/mm and 2.5 kJ/mm. The exposed surface of the samples included the base metal, weld bead, and HAZ. After the immersion test, the exposed surfaces were carefully polished and electrolytically etched in 10% oxalic acid solution at 3 A and 3 V, with a current density of 1 A/cm^2 during 20 s. Pitting in the microstructure of the HAZ was observed using optical microscopy and SEM.

3. Results

3.1. Microstructure of the HAZ regions

The cross-section macrographs with both heat inputs are shown in Figure 1, where the geometry of the fusion line presents an inflection, giving rise to three regions or subzones in the HAZ: close to the sheet edge (A), adjacent to the inflection of the fusion line (B) and below the center of the bead (C). These regions of the HAZ in the welded joint are schematically represented in Figure 2, where the arrows indicate qualitatively the main directions and amount of heat flow during cooling in correspondence with the Rykalin 2D model[24,25].

Figure 3 shows the optical and processed images of the three HAZ regions with both heat inputs. In this figure, the different ferrite grain sizes and HAZ widths are observed in the three selected HAZ regions. Figure 4 shows more clearly these differences because in Figure 3 the scale bar is different for the two heat inputs. This confirm that the cooling rates were significantly different in the three HAZ regions with both heat inputs.

Table 1. Chemical composition of the base metal and the electrode.

Material	C	Si	Mn	Cr	Ni	Mo	N	P	S
UNS S31803(2205)	0.029	0.37	1.79	22.76	5.38	2.96	0.18	0.037	0.0028
Sandvik 22.8.3.L	0.02	0.50	1.60	23.00	9.00	3.20	0.16	≤0.02	≤0.025

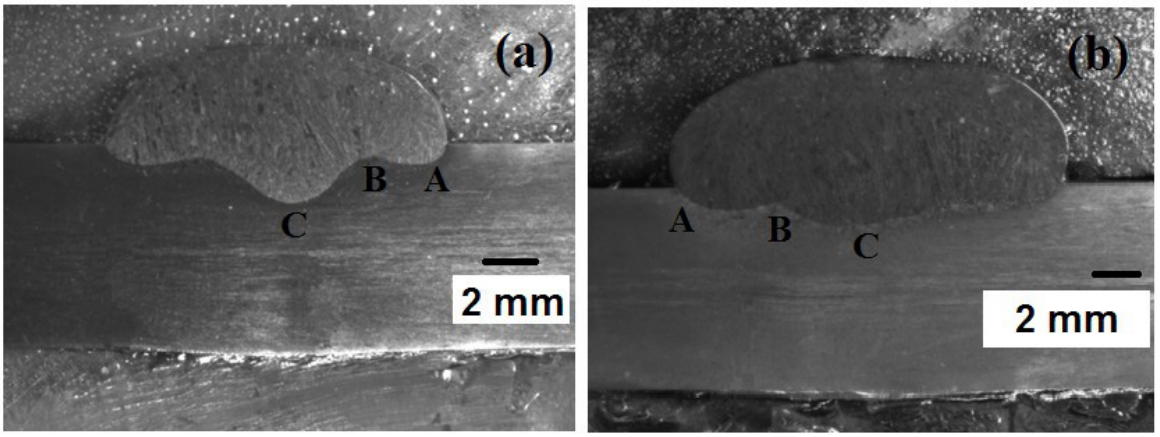

Figure 1. Macrographs of the welded samples. (a) 1.5 kJ/mm, (b) 2.5 kJ/mm.

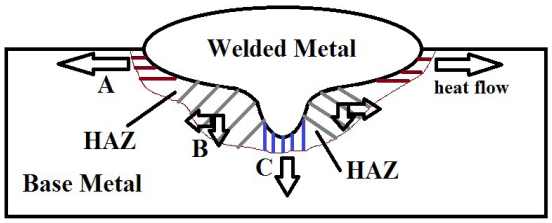

Figure 2. Graphical representation of the different HAZ regions in the cross-section of the weld.

Figure 5 shows the volume fractions of the different austenite morphologies in the HAZ regions with 1.5 and 2.5 kJ/mm respectively.

Figure 5 shows that the HAZ region with a larger ferrite grain size (Figures 3 and 4) showed a lower GBA volume fraction with higher WA and IGA contents. In addition, all HAZ regions of the welds with1.5 kJ/mm showed higher GBA fractions and lower WA and IGA contents, when compared to the 2.5 kJ/mm HAZ regions.

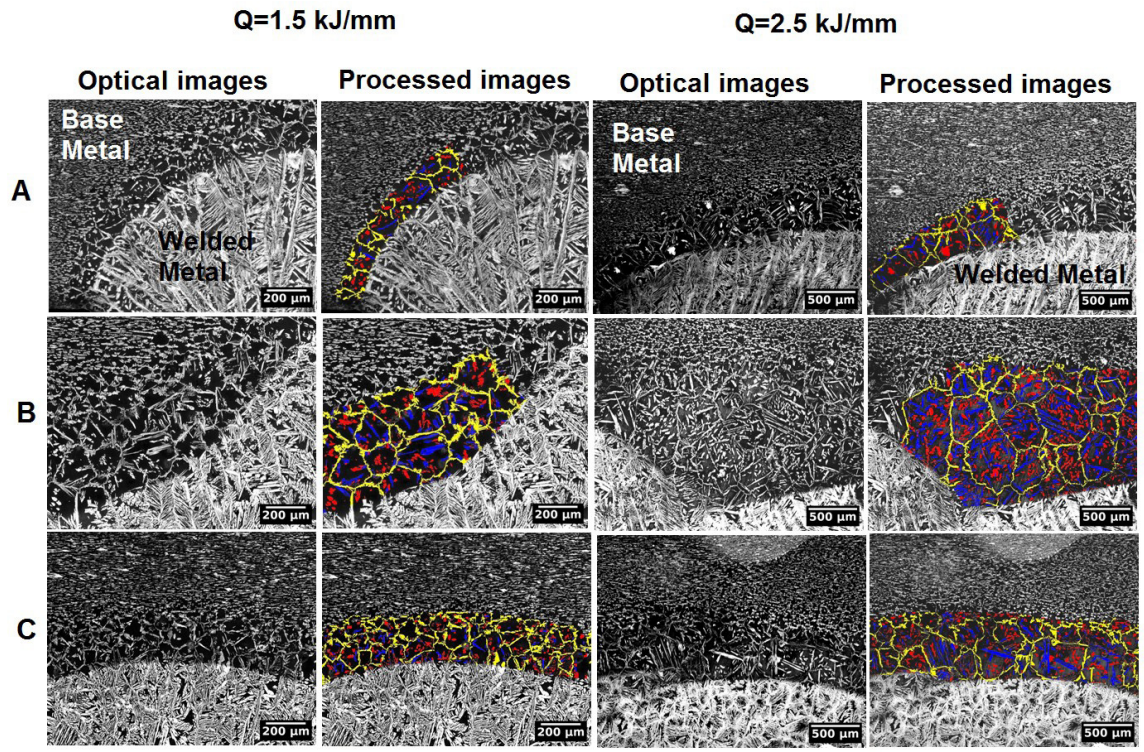

Figure 3. Images of the three HAZ regions. The GBA, WA and IGA, in the processed images, are colored in yellow, blue and red, respectively.

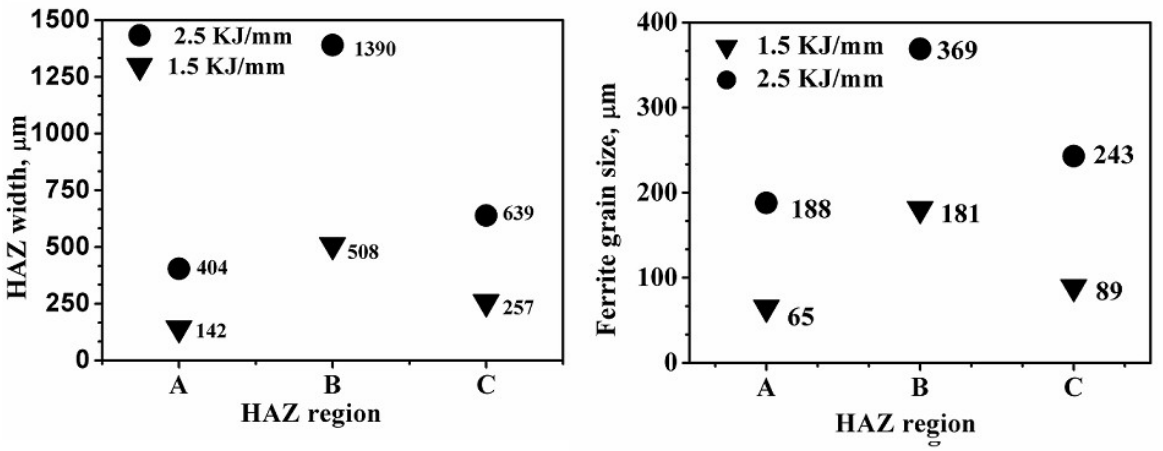

Figure 4. Average values of the HAZ width and the average ferrite grain size in the three HAZ regions of the welded samples obtained with both heat inputs.

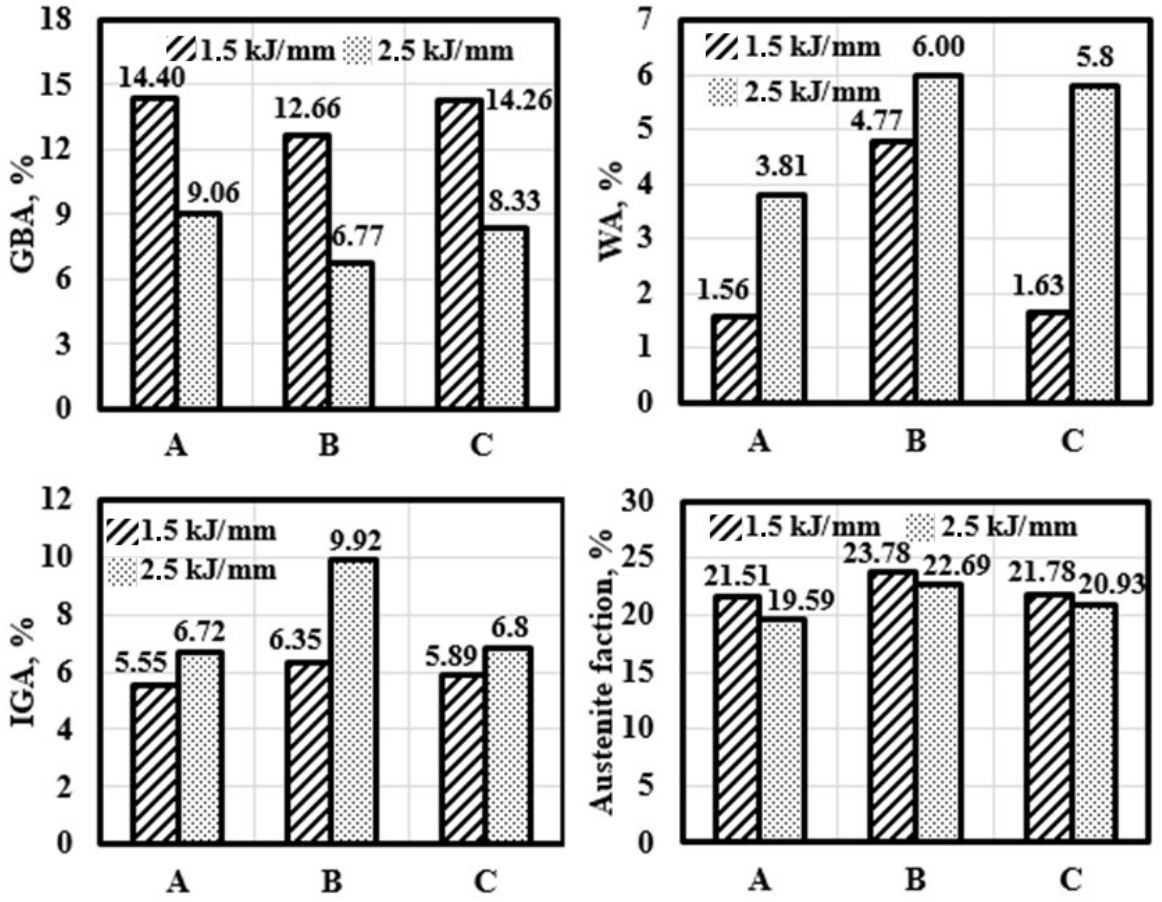

Figure 5. GBA, WA and IGA volume fractions of the HAZ regions with 1.5 and 2.5 kJ/mm. The total austenite volume fractions are also showed in the different HAZ regions.

To obtain a relationship between the heat input Q and the ferrite grain size, equivalent simulated HAZs of the same DSS were performed with a Gleeble thermo-mechanical simulator using five heat inputs[7]. It is known that the ferrite grain growth is controlled by the dissolution of austenite during heating[26]. As the spacing between the austenite grains is small in the base metal of the studied DSS (as-received condition), the ferrite grain growth is insignificant during high heating rates to reach the peak temperature, (~1350 ºC determined by the Thermo-Calc software for this alloy composition). In addition, the short holding time at this temperature (2 s.) do not allow an appreciable growth of the ferritic grain. Therefore, the differences in the ferritic grain sizes at the simulated and real weld HAZs are determined by the cooling rate from the peak temperature up to approximately 1200 ºC. This is because the formation of GBA along the ferrite grain boundaries at approximately 1200 ºC hinders further ferrite grain growth. Hence, it is justified that similar grain sizes between a HAZ region in the welded joint and a simulated HAZ (for a given heat input) have similar cooling times regardless of how the heat was dissipated. An excellent linear fit resulted between the heat input Q and the average ferrite grain size <d> corresponding to five simulated HAZs of the UNS S31803(2205) DSS.

$$Q = 0.0188 * d - 0.5092, \left(R^2 = 0.9949\right). \quad (1)$$

Equivalent heat inputs ($Q_{eq.}$) of the HAZ regions of the real welds (Table 2) can be obtained by replacing the ferrite grain size (d) in equation (1), with that of the real weld HAZs (d^*). The cooling times between T_1=1200 ºC and T_2=800 ºC ($\Delta t_{12/8}$) or between 800-500 ºC ($\Delta t_{8/5}$) are calculated through equation (2) derived from the 2D Rykalin model[25]:

$$\Delta t = \frac{Q_{eq}^2}{4\pi\lambda\rho_c L^2}\left[\frac{1}{(T_2 - T_0)^2} - \frac{1}{(T_1 - T_0)^2}\right] \quad (2)$$

where L=10 mm (plate thickness), T_0=25 ºC the start temperature of the plate, ρ_c=0.005304 J/mm³ ºC the specific heat per unit volume and λ= 0,022 J/mm³ °C the thermal conductivity of the material. Both ρ_c and λ are average values between ambient temperature and solidus temperature[24,25].

3.2. Susceptibility to pitting

Table 3 shows the average values of the main chemical elements in the different phases and austenite morphologies at the HAZ regions. These average values were obtained of three EDS spectra acquired in each HAZ region.

Table 2. Equivalent heat inputs (Qeq), average ferrite grain sizes (d^*), Δt12/8, Δt8/5, ϕ12/8(cooling rate between 1200 ºC and 800 ºC) and ϕ8/5in each HAZ region

HAZ region	d^*, µm	Q_{eq}, kJ/mm	$\Delta t_{12/8}$, s	$\Delta t_{8/5}$, s	$\phi_{12/8}$, ºC/s	$\phi_{8/5}$, ºC/s
Heat input Q=1.5 kJ/mm						
A	65	0.713	3.26	9.59	122.66	31.28
B	181	2.894	53.73	158.05	7.45	1.90
C	89	1.164	8.69	25.57	46.02	11.73
Heat input Q=2.5 kJ/mm						
A	188	3.025	58.70	172.69	6.81	1.74
B	369	6.428	265.05	779.75	1.51	0.38
C	243	4.059	105.69	310.92	3.78	0.96

Table 3. Composition of phases (wt%) and $PREN_{30}$ values in each HAZ region.

Region	Phase	Si	Cr	Mn	Fe	Ni	Mo	N	PREN
UNS S31803(2205)	δ	0.33±0.01	23.26±0.07	1.65±0.02	66.74±0.04	4.82±0.04	3.2±0.04	0.05	35.32
	γ	0.29±0.01	21.35±0.03	1.80±0.03	67.86±0.04	6.50±0.06	2.2±0.05	0.31	37.97
A HAZ 1.5 kJ/mm	δ	0.30±0.01	23.02±0.17	1.60±0.11	66.73±0.18	5.51±0.13	2.94±0.02	0.05	34.22
	GBA	0.32±0.03	22.56±0.08	1.63±0.18	66.62±0.65	6.20±0.68	2.68±0.1	0.51	46.46
	WA	0.34±0.01	22.84±0.31	1.47±0.05	65.10±0.12	7.48±0.31	2.77±0.07	0.49	46.68
	IGA	0.36±0.03	22.69±0.03	1.53±0.09	66.46±0.6	6.09±0.67	2.87±0.08	0.47	46.26
B HAZ1.5 kJ/mm	δ	0.33±0.01	22.75±0.14	1.61±0.03	67.00±0.31	5.32±0.21	2.99±0.04	0.05	34.12
	GBA	0.30±0.03	22.46±0.13	1.57±0.09	66.67±0.73	6.28±0.69	2.71±0.06	0.53	47.24
	WA	0.30±0.01	22.18±0.35	1.66±0.10	66.77±0.41	6.53±0.80	2.56±0.05	0.50	45.53
	IGA	0.27±0.01	22.52±0.09	1.80±0.01	67.40±0.04	5.56±0.04	2.45±0.04	0.46	44.31
C HAZ 1.5 kJ/mm	δ	0.30±0.01	23.02±0.03	1.76±0.11	66.53±0.30	5.44±0.38	2.95±0.06	0.05	34.26
	GBA	0.35±0.06	22.49±0.26	1.68±0.14	65.53±1.04	7.16±0.64	2.79±0.21	0.52	47.17
	WA	0.42±0.04	22.56±0.13	1.60±0.08	64.58±0.03	8.04±0.11	2.79±0.12	0.51	47.06
	IGA	0.36±0.05	22.39±0.25	1.62±0.05	66.49±0.66	6.53±0.69	2.6±0.04	0.47	45.1
A HAZ 2.5 kJ/mm	δ	0.33±0.01	22.94±0.02	1.69±0.03	67.02±0.09	5.06±0.08	2.96±0.03	0.05	34.21
	GBA	0.33±0.01	22.39±0.08	1.74±0.03	67.44±0.09	5.89±0.04	2.54±0.04	0.55	47.27
	WA	0.31±0.03	22.59±0.01	1.80±0.04	67.35±0.05	5.63±0.11	2.63±0.12	0.53	47.16
	IGA	0.32±0.01	22.77±0.23	1.67±0.04	67.48±0.22	5.42±0.25	2.65±0.23	0.48	46.03
B HAZ 2.5 kJ/mm	δ	0.32±0.01	22.78±0.09	1.70±0.02	67.08±0.08	5.22±0.03	2.9±0.02	0.05	33.85
	GBA	0.32±0.01	22.57±0.51	1.70±0.11	67.19±0.23	5.50±0.50	2.71±0.32	0.58	48.91
	WA	0.33±0.02	22.44±0.13	1.77±0.04	67.35±0.07	5.62±0.12	2.49±0.02	0.53	46.55
	IGA	0.31±0.01	22.51±0.03	1.67±0.01	67.29±0.01	5.50±0.07	2.73±0.07	0.47	45.47
C HAZ 2.5 kJ/mm	δ	0.30±0.01	22.92±0.01	1.66±0.01	69.98±0.01	5.15±0.07	2.99±0.02	0.05	34.29
	GBA	0.32±0.02	22.27±0.24	1.72±0.05	67.36±0.16	5.76±0.19	2.56±0.13	0.57	47.82
	WA	0.30±0.01	22.6±0.14	1.70±0.05	67.09±0.08	5.68±0.12	2.63±0.08	0.52	46.82
	IGA	0.31±0.02	22.58±0.05	1.72±0.02	67.19±0.03	5.55±0.05	2.65±0.05	0.48	45.63

The uncertainty was calculated by $\sigma/(n)^{1/2}$, where σ is the standard deviation and n=3.

It is remarkable partition of the elements between phases. In the base metal (BM), Ni and Mn are higher in austenite, while Cr and Mo are higher in ferrite. The ferrite phase in all HAZ regions has lower Cr and Mo contents with respect to the BM. Collaterally, the contents of these elements in austenite are higher in the HAZs than in austenite of the BM. The Ni amount increased in ferrite of the HAZs, when compared to the BM. The IGA particles show the lowest Ni content with respect to other austenite morphologies in the HAZ regions. The nitrogen content was assumed 0.05% in ferrite (maximum solubility in this phase)[4,15]. The Thermo-Calc software with the Steel/Fe TCFE8 thermodynamic database was used to estimate the nitrogen content in the different austenite morphologies. The procedure consisted of estimating the equilibrium nitrogen content, using Thermo Calc, for each experimentally determined volume fraction of austenite within the temperature range where it approximately forms. First, the nitrogen content was determined for the GBA volume fraction, first austenite morphology to form, at approximately 1200 ºC. Subsequently, the nitrogen content was determined for the GBA+WA volume fraction, and by conservation of substance, the nitrogen content in WA was calculated. This procedure was repeated adding the IGA volume fraction.

Table 3 also show the $PREN_{30}$ values in each HAZ region: $PREN_{30}$=%Cr+3.3%Mo+30%N[4,15].

Critical pitting temperature (CPT) allows for the evaluation of corrosion resistance of DSS. Therefore, ASTM

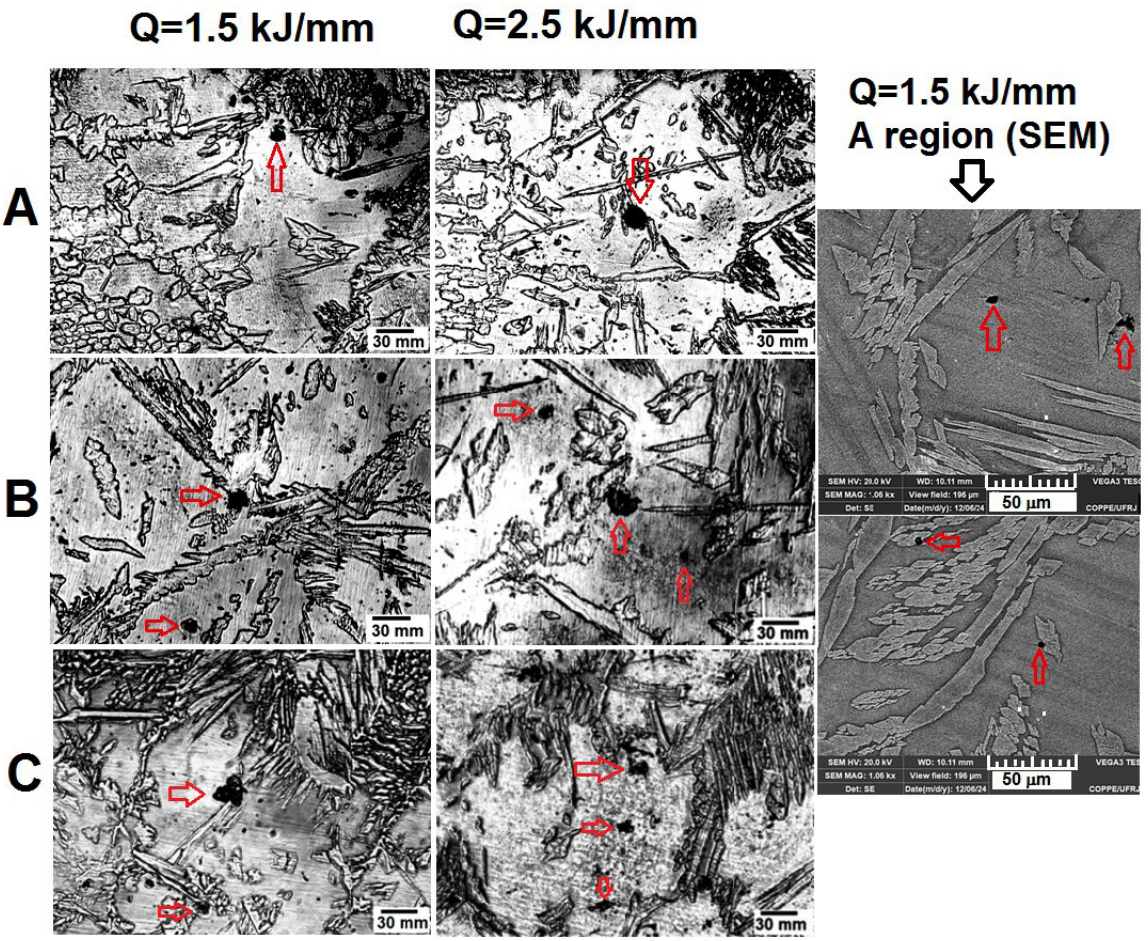

Figure 6. Optical images of the HAZ regions after the immersion testing in an acidified ferric chloride solution. SEM images of the A HAZ region with 1.5 kJ/mm showing metastable pits. The arrows indicate the place where the pits are originated.

G48 in its method C establishes an equation to estimate the minimum critical pitting temperature (CPTmin) based on the chemical composition of the alloy at room temperature[22]. According to this standard, the equation for this alloy is: CPTmin.= 2.5%Cr+7.6%Mo+31.9%N-41. Although the CPTmin value calculated by this equation may not coincide with the CPT of the alloy that is determined experimentally, it allows an initial assessment of the resistance to pitting corrosion of phases in this alloy with different chemical compositions. Applying this equation to the present UNS S31803 DSS (Table 1) a value of 44.1 ºC is obtained. This result is consistent with the values reported by[19,27], who experimentally obtained a CPT value of 44.8 °C[19] and between 40 °C and 45 ºC[27] for the DSS UNS S31803 using an acidified ferric chloride solution according to ASTM G48. As the ferrite in the HAZ is the phase most susceptible to pitting corrosion (Table 3), the CPTmin values of this phase were calculated using the compositions given in Table 3. The results were: 40.5 ºC, 40.2 ºC and 40.6 ºC for A, B, and C HAZ regions of the welded joint with a heat input of 1.5 kJ/mm. Similarly, for the A, B and C HAZ regions of the welded joint with a heat input of 2.5 kJ/mm, the CPTmin values of ferrite were: 40.4 ºC, 39.6 ºC and 40.6 ºC respectively.

The ferrite CPTmin values in the A and C HAZ regions are similar with both heat inputs. For the B HAZ regions, the CPTmin values were slightly lower, especially for the B HAZ region of the welded joint with 2.5 kJ/mm as heat input.

Figure 6 shows the optical and SEM images where small pitting (or metastable pitting) are observed in the microstructure, preferentially within the ferrite grains and at the IGA-matrix interface.

4. Discussion

The austenite morphologies (GBA, WA and IGA) were observed in the different HAZ regions (Figure 3). No partially dissolved austenite was evidenced, indicating that the austenite was formed from a fully ferritic matrix. During cooling ferrite transforms into austenite on the ferrite grain boundaries. The first nucleated austenite (~1200 ºC) is known as allotriomorphic austenite (GBA). The GBA along the ferrite grain boundaries hinders the ferrite grain growth consuming nitrogen[6,7]. At low temperatures, (1000-800 ºC) the WA nucleates from the GBA towards the ferrite grain with an specific orientation relationship with ferrite matrix. The WA laths are larger with larger ferrite grain sizes[6,7,12,28].

The WA morphology formed at high temperature has a better partition of the chemical elements with the matrix, while the one formed at lower temperatures is fragmented to balance its composition[5,28]. The IGA nucleates and grows at higher undercooling after the WA formation, given the lower nitrogen content in the matrix and limited nucleation sites, as depicted in Figure 3. In this Figure is observed that the ferrite grains where the WA volume fraction predominates, the IGA volume fraction do not have a strong presence and vice versa. The IGA nucleated at lower temperatures develops more interfaces with specific orientation relationships (OR) (Kurdjumov-Sachs/Nishiyama-Wassermann) than the IGA formed at higher temperatures[7,29].

The results (Figures 4 and 5) show that the ferrite-to-austenite transformation has a dual dependence with the heat input. On one hand, higher heat inputs promote more WA and IGA, while, on the other hand, higher heat inputs favor the growth of the ferrite grain size, decreasing the GBA fraction. Thus, the ferrite-to-austenite transformation is governed by the cooling time of each HAZ region. The total austenite fraction of each HAZ region increases with the decrease of the cooling rate, in agreement with[2-4,7].

The effect of different heat inputs on the microstructure and on the localized corrosion behavior of the simulated and real HAZ in the UNS S31803 duplex stainless steel (DSS) has been widely discussed in the literature. Most articles about duplex steels explain the resistance to localized corrosion in the HAZ considering only the total austenite and ferrite volume fractions. Few articles qualitatively describe the influence of cooling rate on the change of the different morphological forms of austenite in the HAZ of this DSS showing contradictory results[3-5,10,30,31]. Thus, the quantification of the austenite morphologies and their compositions, Figures 3, 4, 5 and Table 3, allow a correct assessment of how these volume fractions influence the susceptibility to corrosive attack in each region of the HAZ through the PREN values.

As described in Table 3, the PREN of the ferrite is lower than of the austenite in the BM, due to a higher N content in austenite. The PREN of the GBA and WA in the A and C HAZ regions, do not show significant variations. The formation of these austenite morphologies in the A and C regions had similar cooling rates, consuming the nitrogen around them. The most significant variations in the PREN for the austenite morphologies occurred in the B regions, which presented the lowest cooling rate, favoring the partitioning of the main chemical elements between the austenite morphologies and, therefore, greater variations in the PREN values. Given that the equilibrium between the austenite morphologies in all HAZ regions is not obtained, their PREN values are higher in the HAZ regions than in the BM austenite. On the contrary, the ferrite PREN in the base metal is higher than the PREN corresponding to the ferrite in the different HAZ regions. GBA had the highest PREN, in comparison to the other austenite morphologies due to its higher nitrogen content. IGA had the lower PREN values than other austenite morphologies. As observed in Figure 5 and Table 3, region B in both HAZs is the most susceptible to pitting corrosion because it has a higher volume fraction of IGA with the lowest PREN value. This region of the HAZ is also characterized by a larger ferritic grain size and a lower GBA volume fraction, which increases susceptibility to corrosive attack, as will be detailed later.

Figure 4 shows the increase of the HAZ width and the ferrite grain size with the heat input. Furthermore, Figure 5 shows that the total ferrite fractions in each particular HAZ region do not present significant differences. The above leads to the consideration that the increase in the area of the HAZ region, as a consequence of the growth of the ferrite grain size, constitutes an aspect that contributes to the increase in the pitting corrosion rate with the heat input. It has been reported that ferrite grain growth increases susceptibility to localized corrosive attack due to the precipitation of chromium nitrides in the central region of the grains[1]. Other authors report that small grain sizes improve the formation and adhesion of the protective film by increasing the density of boundaries[32].

The microstructures after the immersion testing in acidified ferric chloride solution revealed pits mainly inside the ferrite grains or at the IGA-ferrite interfaces, Figure 6. Since the nitrogen content for all austenite morphologies is higher than in ferrite, they have higher PREN values and are better protected against pitting[1]. In addition, the presence of Cr_2N nitrides inside the ferrite grains constitutes suitable sites for the pit nucleation[3,7]. It is recognized in the literature that the nitride precipitation generates chromium depleted regions around the Cr_2N within ferrite grains and at the austenite-ferrite boundaries[17,33]. These chromium-depleted regions can cause a further decrease in the PREN, further contributing to pitting. However, recent reports[34,35] indicate that a fine dispersion of Cr_2N does not appear to act as an initial site for localized corrosion. The susceptibility of Cr_2N as an initial site for pitting corrosion will depend on its size, distribution, and the surrounding chemical environment. The elimination of chromium-depleted zones around nitrides depend on the particle spacing, the diffusivity of chromium, and the cooling rate[26].

When the cooling rate is significantly high, Cr_2N nucleation could be associated with the previous CrN[2], since CrN precipitation is more favorable, while chromium diffusion is more difficult. The presence of Cr_2N and CrN is reported in[2,4,12,36,37]. For a faster cooling, the CrN fraction increases. When the cooling rate is higher than 100 °C/s, the CrN dominates[13], decreasing the pitting formation, as the Cr depletion at the vicinities of CrN particles is small, reducing its effect on pitting corrosion[13].

Table 2 shows that the A HAZ region with 1.5 kJ/mm had a cooling rate of 122.66 °C/s. Thus, the nitrides precipitated in this HAZ region should be mostly CrN, with a lower tendency for pits. In the B and C HAZ regions (for both heat inputs) the cooling rates were lower than 100 °C/s (Table 2). Therefore, Cr_2N nitrides are favored in these regions of the HAZs.

So, the diffusion distances of the Cr and N atoms into the ferrite grains were calculated between 1200 and 800 ºC in the different HAZ regions[2,6,7,12,38]:

$$x = \sqrt{\int_0^{tf} D_{if}\left(T\right) dt}\ , \tag{3}$$

t_f: cooling time, $D_{if}(T)$: diffusion coefficient, expressed as:

$$D_{if}(T) = D_0 \exp\left(-\frac{E}{RT}\right), \quad (4)$$

with D_o =1.13 x 10^{-6} m^2/s for N and D_o =2.3 x 10^{-4} m^2/s for Cr. The activation energies for N and Cr are E = 83(1-14.03/T) kJ/mol and E = 239 kJ/mol respectively. Temperature in Equation (4) is expressed by the relation $T=T_o-\phi t$, where T_o is the starting temperature (1200 °C) and ϕ(°C/s) the cooling rate between the two temperatures. Table 4 shows the calculated diffusion distances for nitrogen and chromium atoms in ferrite corresponding to different HAZ regions. The Cr diffusion distance is significantly lower than N. Therefore, chromium recovery in ferrite around Cr_2N nitride may be retarded, which locally decreases its PREN.

In Table 4, the nitrogen diffusion distances for all HAZ regions are of the same order as the grain diameters. Therefore, the conditions for nitride formation inside the ferrite grains, with respect to N, in all HAZ regions (for both heat inputs) are similar. As can be seen in Figure 4, the total austenite fractions in all HAZ regions with both heat inputs are lower than the ferrite fractions. In Table 4 it is observed that the A HAZ region, with 1.5 kJ/mm, has the shortest N diffusion distance, when compared to the other regions. The A region also has the lowest fraction of IGA+WA (Figure 5), and the highest Cr content in ferrite (Table 3). Consequently, in the ferrite in the A HAZ region, the precipitation of Cr_2N could be significant in addition to the CrN,

Figure 7 shows the bright field TEM-STEM images of the A and B HAZ regions with lower heat input (1.5 kJ/mm).

Table 4. Ferrite grain size (d*), Δt12/8, ϕ12/8 and diffusion distances (1200- 800 ºC) of N and Cr in the ferrite grains (Λ_N, Λ_{Cr}) for the three HAZ regions.

HAZ region	d* µm	Δt12/8 s	ϕ12/8 °C/s	Λ_N µm	Λ_{Cr} µm
Q=1.5 kJ/mm					
A	65	3.26	122.66	43	0.65
B	181	53.73	7.45	175	2.60
C	89	8.69	46.02	70	1.06
Q=2.5 kJ/mm					
A	188	58.70	6.81	183	2.70
B	369	265.05	1.51	388	5.90
C	243	105.69	3.78	245	3.70

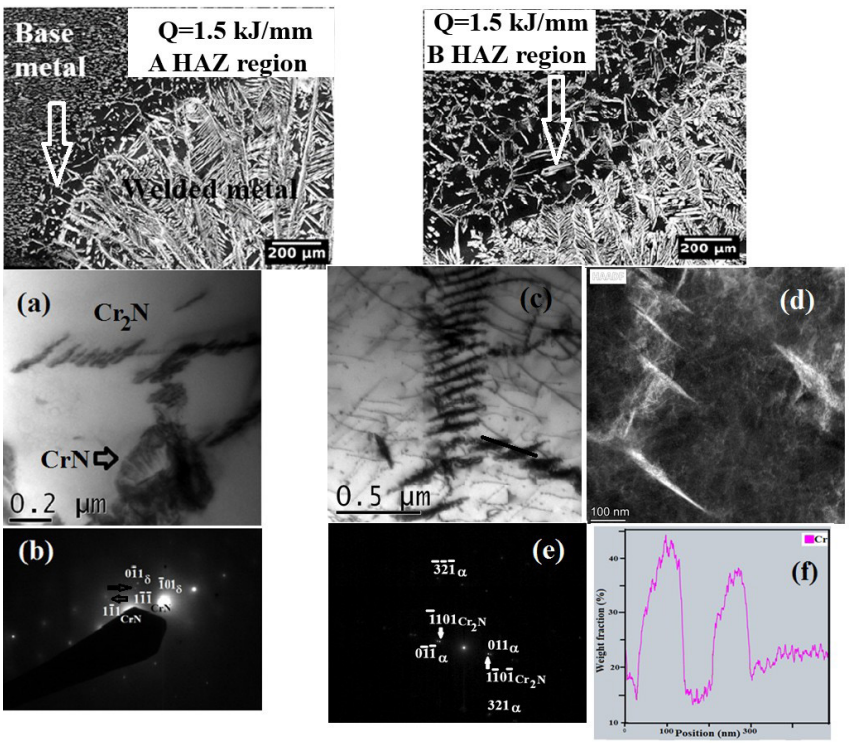

Figure 7. Bright field TEM-STEM images of the A and B HAZ regions (1.5 kJ/mm). CrN (a) and Cr_2N (c,d) are evidenced by SAED patterns in (b) and (e). Line scan between nitrides in (f) shows de Cr-depleted region around the nitride particles. The arrows in HAZ show the locations of the thin foils.

The A region shows both nitrides CrN and Cr_2N (Figure 7(a, b)), while in the B one only Cr_2N persists (Figure 7(c, d, e)). The dispersion and relative sizes of the Cr_2N nitrides are also highlighted. Nitride chains can be observed along the grain sub-boundaries in the B HAZ region (Figure 7(c)). These nitride chains favor the existence of nearby Cr-depleted regions as shown in Figure 7(f) making the B region more prone to pitting corrosion.

The formation of rod-like Cr_2N and sheet-like CrN in simulated HAZ of UNS S31803(2205) DSS at two cooling rates, 150 °C/s and 40 °C/s, was investigated[2], showing that the density and size of the Cr_2N is higher for the lower cooling rate, while the density of the CrN is higher for the higher cooling rate. The C HAZ region of the welded sample with 1.5 kJ/mm had a cooling rate (46.02 ºC/s) similar to[2] (40 ºC/s). Then, it is assumed that both types of nitrides (Cr_2N and CrN) can exist in C region. The other HAZ regions with lower cooling rates are prone only for the Cr_2N precipitation.

The aforementioned justifies different fractions and sizes of Cr_2N in the HAZ regions with 1.5 kJ/mm. The A region, with the highest cooling rate (122.66 ºC/s), is believed to present a higher fraction of CrN and a few and small dispersed particles of Cr_2N. In the C region (46.02 ºC/s), the fraction of less dispersed and more coalesced Cr_2N increases, while in region B, chains of coalesced Cr_2N predominates as shown in Figure 7(c). The spacing between the Cr_2N particles in these chains is relatively small (~50 nm), which creates Cr-depleted regions around them as it is shown in Figure 7(f). In this Figure 7(f) the Cr content around the nitrides, in this chain, is much lower than the nominal Cr concentration (23 wt%) of the alloy. At 2.5 kJ/mm, the cooling rates of the HAZ regions are much lower than at a heat input of 1.5 kJ/mm. For this reason, the susceptibility to corrosive attack of their HAZ regions showed no significant differences. Thus, in the HAZ with the lowest heat input, the greatest variations in corrosion resistance were detected between its different regions. The B HAZ regions had the lowest corrosion resistance being more intense for the heat input of 2.5 kJ/mm. As evidenced in Figure 6, the pits are larger and more frequent in the HAZ regions with lower cooling rate, while for the A HAZ region with higher cooling rate, the pits are smaller and less frequent.

Another important aspect for the HAZ with heat input of 2.5 kJ/mm, that contributed to a lower corrosion resistance, is the higher amount of incoherent δ/γ interfaces, when compared to 1.5 kJ/mm. As shown in Figure 5, the IGA fractions in the three HAZ regions with 2.5 kJ/mm are higher than the same regions with 1.5 kJ/mm. According to[4,29], the IGA formed at lower cooling rates ($\Delta t_{8/5} \geq 80$ s) presents a more random interfaces with the ferrite matrix, favoring the emergence of pits. In the B HAZ region, the higher fraction of IGA particles, Figure 5, with lower PREN and higher fraction of δ/γ incoherent interfaces favors the initiation and growth of pitting.

As shown in Figure 6, small pits with different sizes and densities appear depending on the HAZ region and the local heat input; these differences are more pronounced with lower heat inputs. All HAZ regions subjected to a heat input of 2.5 kJ/mm exhibit lower pitting corrosion resistance compared to the corresponding regions with a heat input of 1.5 kJ/mm. Among the subzones of the HAZ, region B is the most susceptible to pitting corrosion due to the presence of coalesced Cr_2N chains and a higher volume fraction of IGA particles with a predominance of incoherent boundaries.

5. Conclusions

Based on the analysis of the HAZs in welds of DSS using GMAW, the following conclusions are considered:

- In single-pass bead-on-plate GMAW welds using an argon-rich shielding gas mixture, three regions appear in the HAZ along the fusion line due to different local cooling rates, related to different equivalent heat inputs.
- The volume fractions of the different austenite morphologies in the HAZ regions are determined by the specific cooling conditions of each zone. A HAZ region with a slow cooling rate induces ferrite grain growth, which decreases the GBA fraction and increases the WA and IGA contents.
- The cooling rate of approximately 122 °C/s in the A HAZ region of the welded joint with 1.5 kJ/mm as heat input, promotes the predominance of CrN and a smaller fraction of Cr_2N, while in the C HAZ subzone, both nitrides are favored. In the B HAZ region, the precipitated nitrides are mainly Cr_2N. These nitrides appear forming chains in the ferrite grain sub boundaries. The small spacing between Cr_2N particles in these chains observed in the B HAZ region caused a local decrease in the PREN around the particles (Cr-depleted zones) favoring pitting corrosion. For welded joint with the heat input of 2.5 kJ/mm, all the HAZ regions showed a dominant precipitation of Cr_2N.
- The B HAZ regions (wide zone) have a higher fraction of IGA particles with incoherent IGA-ferrite interfaces and lower nitrogen content, which leads to a more pronounced susceptibility to localized corrosive attack.

6. Acknowledgments

The authors wish to thank FAPERJ (E-26/202.757/2023[287514] and 26/201-535/218) and CAPES (PVE 88881.064968/2014-01) for the financial support. We acknowledge the reviewers for their insightful criteria and suggestions.

7. References

1. Ogawa T, Koseki T. Effect of composition profiles on metallurgy and corrosion behavior of duplex stainless steel weld metals. Weld J. 1989;5:181-91.
2. Liao J. Nitride precipitation in weld HAZs of duplex stainless steel. ISIJ Int. 2001;41(5):460-7. https://doi.org/10.2355/isijinternational.41.460.
3. Liou HY, Hsieh RI, Tsai WT. Microstructure and pitting corrosion in simulated heat-affected zones of duplex stainless steels. Mater Chem Phys. 2002;74(1):33-42. https://doi.org/10.1016/S0254-0584(01)00409-6.
4. Yang Y, Yan B, Li J, Wang J. The effect of large heat input on the microstructure and corrosion behavior of simulated heat affected zone in 2205 duplex stainless steel. Corros Sci. 2011;53(11):756-3763. https://doi.org/10.1016/j.corsci.2011.07.022.

5. Wu TH, Wang JJ, Li HB, Jiang ZH, Liu CM, Zhang HY. Effect of heat input on austenite microstructural evolution of simulated heat-affected zone in 2205 duplex stainless steel. J Iron Steel Res Int. 2019;26(5):435-41. https://doi.org/10.1007/s42243-018-0134-z.
6. Varbai B. Heat-affected zone characterization of X2CrNiN22-2 lean duplex stainless steel by metallographic and electrochemical techniques. J Mater Eng Perform. 2023;32(24):11240-9. https://doi.org/10.1007/s11665-023-08807-3.
7. Morales EV, Pozo JA, Olaya L, Kassab E, Ponciano JAC, Ghavami K, et al. Remarks on the evolution and performance of the different austenite morphologies at the simulated HAZs of a 2205 duplex stainless steel. J Mater Res Technol. 2019;8(5):3936-49. https://doi.org/10.1016/j.jmrt.2019.07.002.
8. Morales EV, Betancourt G, Olaya L, Bott IS. Some insight on the heat-affected zone strengthening mechanisms in duplex stainless steels. Mater Res. 2022;25:e20210553. https://doi.org/10.1590/1980-5373-mr-2021-0553.
9. Tehovnik F, Arzenšek B, Arh B, Skobir D, Pirnar B, Žužek B. Microstructure evolution in SAF 2507 super duplex stainless steel. Mater Technol. 2011;45(4):339-45.
10. Muthupandi V, Srinivasan PB, Seshadri SK, Sundaresan S. Effect of weld metal chemistry and heat input on the structure and properties of duplex stainless-steel welds. Mater Sci Eng A. 2003;358(1-2):9-16. https://doi.org/10.1016/S0921-5093(03)00077-7.
11. Sieurin H, Sandström R. Austenite reformation in the heat-affected zone of dúplex stainless steel 2205. Mater Sci Eng A. 2006;418(1-2):250-6. https://doi.org/10.1016/j.msea.2005.11.025.
12. Morales EV, Cruz-Crespo A, Pozo-Morejón JA, Oria JVM, Araujo LS, Bott IS. Microstructural characteristics of different heat affected zones in welded joints of UNS S32304 duplex stainless steel using the GMAW process: analysis of the pitting corrosion resistance. Corros Rev. 2023;11:1-13. https://doi.org/10.1515/corrrev-2023-0061.
13. Omura T, Kushida T, Komizo Y. Nitrogen distribution on rapid solidification in laser welded duplex stainless steels. Weld Int. 2000;14(4):288-94. https://doi.org/10.1080/09507110009549181.
14. Xavier CR, Guimarães H, De Castro JA. An experimental and numerical approach for the welding effects on the duplex stainless steel microstructure. Mater Res. 2015;18(3):489-502. https://doi.org/10.1590/1516-1439.302014.
15. Paulraj P, Garg R. Effect of intermetallic phases on corrosion behavior and mechanical properties of duplex stainless steel and super-duplex stainless steel. Adv Sci Technol Res Jour. 2015;9(27):87-105. https://doi.org/10.12913/22998624/59090.
16. Boschetti-Pereira H, Carvalhaes-Pimentel TH, Da Silva CA, Panossian Z, Farias de Azevedo CR. Influence of welding energy on intergranular and pitting corrosion susceptibility of UNS S32205 duplex stainless-steel joints. Mater Res. 2022;25(Suppl 1):e20210488. https://doi.org/10.1590/1980-5373-mr-2021-0488.
17. Zhang Z, Jing H, Xu L, Han Y, Zhao L, Zhang J. Influence of microstructure and elemental partitioning on pitting corrosion resistance of duplex stainless steel welding joints. Appl Surf Sci. 2017;394:297-314. https://doi.org/10.1016/j.apsusc.2016.10.047.
18. Nowacki J, Łukojć A. Structure and properties of the heat-affected zone of duplex steels welded joints. J Mater Process Technol. 2005;164–165:1074-81. https://doi.org/10.1016/j.jmatprotec.2005.02.243.
19. Chaofang D, Hong L, Kui X, Ting S, Qian L, Xiaogang L. Effect of temperature and Cl- concentration on pitting of 2205 duplex stainless steel. J Wuhan Univ Technol Mater Sci Ed. 2011;26(4):641-7. https://doi.org/10.1007/s11595-011-0283-4.
20. Miranda-Pérez AF, Rodríguez-Vargas BR, Calliari I, Pezzato L. Corrosion resistance of GMAW duplex stainless steels welds. Materials. 2023;16(5):1847. https://doi.org/10.3390/ma16051847.
21. Kordatos JD, Fourlaris G, Papadimitriou G. The effect of cooling rate on the mechanical and corrosion properties of SAF 2205 (UNS 31803) duplex stainless steel welds. Scr Mater. 2001;44(3):401-8. https://doi.org/10.1016/S1359-6462(00)00613-8.
22. ASTM: American Society for Testing and Materials. ASTM G48-11: standard test methods for pitting and crevice corrosion resistance of stainless steels and related alloys by use of ferric chloride solution. West Conshohocken: ASTM International; 2015. http://dx.doi.org/https://doi.org/10.1520/G0048-11R15.
23. ASTM: American Society for Testing and Materials. ASTM E3-11: standard guide for preparation of metallographic specimens. West Conshohocken: ASTM International; 2011.
24. Poorhaydari K, Patchett BM, Ivey DG. Estimation of cooling rate in the welding of plates with intermediate thickness. Weld J. 2005;84(10):149s-55s.
25. Pozo-Morejón JA, Guimaraes de Souza LF, Guerra T, Morales EV, Bott IS, Cruz-Crespo A, et al. Heat inputs adjustment corresponding to the HAZ cooling times in GMAW on 2205 duple steel using finite element simulation. Soldag Insp. 2018;23(3):413-22. https://doi.org/10.1590/0104-9224/si2303.10.
26. Atamer S, King JE. Superduplex stainless steels. Part 1. Heat affected zone microstructures. Mater Sci Technol. 1992;8(10):896-911. https://doi.org/10.1179/mst.1992.8.10.896.
27. Hoseinpoor M, Momeni M, Moayed MH, Davoodi A. EIS assessment of critical pitting temperature of 2205 duplex stainless steel in acidified ferric chloride solution. Corros Sci. 2014;80:197-204. https://doi.org/10.1016/j.corsci.2013.11.023.
28. Ohmori Y, Nakai K, Ohtsubo H, Isshiki Y. Mechanism of Widmanstätten austenite formation in a δ/γ duplex phase stainless steel. ISIJ Int. 1995;35(8):969-75. https://doi.org/10.2355/isijinternational.35.969.
29. Haghdadi N, Cizek P, Hodgson PD, Tari V, Rohrer GS, Beladi H. Effect of ferrite-to-austenite phase transformation path on the interface crystallographic character distribution in a duplex stainless steel. Acta Mater. 2018;145:196-209. https://doi.org/10.1016/j.actamat.2017.11.057.
30. Wang S-H, Chiu P-K, Yang J-R, Fang J. Gamma (γ) phase transformation in pulsed GTAW weld metal of duplex stainless steel. Mater Sci Eng A. 2006;420(1-2):26-33. https://doi.org/10.1016/j.msea.2006.01.028.
31. Kuruda T, Ikeuchi K, Kitagawa Y. Role of austenite in weld toughness of superduplex stainless steel. Weld World. 2006;49(5-6):29-33. https://doi.org/10.1007/BF03263407.
32. Ralston KD, Birbilis N. Effect of grain size on corrosion. A review. Corrosion. 2010;66(7):1-13. https://doi.org/10.5006/1.3462912.
33. Sucupira DC, Frankel GS, Lins VFC. Pitting corrosion of welds in S32304 lean duplex stainless steel. Mater Corros. 2016;67(5):440-8. https://doi.org/10.1002/maco.201508502.
34. Haghdadi N, Laleh M, Chen H, Chen Z, Ledermueller C, Liao X, et al. On the pitting corrosion of 2205 duplex stainless steel produced by laser powder bed fusion additive manufacturing in the as-built and post-processed conditions. Mater Des. 2021;212:110260. https://doi.org/10.1016/j.matdes.2021.110260.
35. Bettini E, Kivisäkk U, Leygraf C, Pan J. Study of corrosion behavior of a 22% Cr duplex stainless steel: influence of nano-sized chromium nitrides and exposure temperature. Electrochim Acta. 2013;113:280-9. https://doi.org/10.1016/j.electacta.2013.09.056.
36. Jargelius-Pettersson RFA, Hertzman S, Szakalos P, Ferreira PJ. Proceedings in duplex stainless steels '94. Glasgow: TWI; 1995. p. 461-72. (vol. 2).
37. Pettersson N, Pettersson RF, Wessman S. Precipitation of chromium nitrides in the super duplex stainless steel 2507. Metall Mater Trans, A Phys Metall Mater Sci. 2015;46(3):1062-72. https://doi.org/10.1007/s11661-014-2718-y.
38. Kobayashi S, Nakai K, Ohmori Y. Decomposition processes of δ-Ferrite during continuous heating in a 25Cr–7Ni–0.14N stainless steel. ISIJ Int. 2000;40(8):802-8. https://doi.org/10.2355/isijinternational.40.802.

Data Availability

All experimental data have been presented in the text of the article.